small methods
www.small-methods.com

Ultrasensitive Molecule Detection Based on Infrared Metamaterial Absorber with Vertical Nanogap

Inyong Hwang, Mingyun Kim, Jaeyeon Yu, Jihye Lee, Jun-Hyuk Choi, Su A. Park, Won Seok Chang, Jongwon Lee, and Joo-Yun Jung**

Surface-enhanced infrared absorption (SEIRA) spectroscopy is a powerful methodology for sensing and identifying small quantities of analyte molecules via coupling between molecular vibrations and an enhanced near-field induced in engineered structures. A metamaterial absorber (MA) is proposed as an efficient SEIRA platform; however, its efficiency is limited because it requires the appropriate insulator thickness and has a limited accessible area for sensing. SEIRA spectroscopy is proposed using an MA with a 10 nm thick vertical nanogap, and a record-high reflection difference SEIRA signal of 36% is experimentally achieved using a 1-octadecanethiol monolayer target molecule. Theoretical and experimental comparative studies are conducted using MAs with three different vertical nanogaps. The MAs with a vertical nanogap are processed using nanoimprint lithography and isotropic dry etching, which allow cost-effective large-area patterning and mass production. The proposed structure may provide promising routes for ultrasensitive sensing and detection applications.

1. Introduction

Infrared (IR) absorption spectroscopy employing the vibrational signatures of substances is a powerful method for label-free and nondestructive identification because the vibrational properties of analytes are directly linked to their molecular constituents and chemical bonds.[1] In particular, Fourier transform infrared (FTIR) spectroscopy based on IR absorption is widely used in basic research and industrial fields, such as pharmacy, safety, environmental monitoring, food, and general substance identification. However, because fingerprint vibrations of molecules in the mid-IR range intrinsically have low-absorption cross sections, a large quantity of the sample is required for detection and identification.[2] Therefore, the use of conventional IR absorption spectroscopy based on the Beer–Lambert law is limited when the analysis of a small quantity of analyte, such as a monolayer, is required. Surface-enhanced IR absorption (SEIRA) spectroscopy was proposed as a method to mitigate this limitation. In this method, the fingerprint vibration of analyte molecules is amplified through coupling with highly enhanced and confined electromagnetic near-fields induced in engineered surfaces or structures.[3–7] After the first experimental demonstration of SEIRA based on resonant coupling using plasmonic nanorods, various types of plasmonic or dielectric resonator structures for SEIRA studies in the mid-IR range were reported, such as split-ring resonators,[8] fan-shaped nanoantennas,[9] nanoslits,[10,11] nanoantennas on pedestals,[12–15] co-axial resonators,[16–18] elliptical dielectric nanoresonators,[19,20] and metamaterial absorbers (MAs).[14,21–27] In recent studies, it was reported that these SEIRA structures can be used to detect biomolecules such as protein A/G and immunoglobulin G (IgG) antibody,[12] bovine serum albumin,[23] and hemoglobin.[28] Because most resonant SEIRA structures use near-field enhancement induced in the in-plane nanometer-sized gap, high-precision fabrication equipment is required, such as e-beam lithography; thus, large-area patterning is limited and costly. Recently, a promising SEIRA study was proposed using the bound states in the continuum (BIC) phenomenon of dielectric resonators with high quality (Q) factors;[19,20] however, this approach also has limitations regarding the fabrication and analysis of multiple pattern arrays using a costly high-precision fabrication process.

Among the various proposed structural platforms, MAs have also demonstrated remarkable SEIRA signal enhancement. MAs composed of metal–insulator–metal configuration are generally designed with a dielectric spacer layer sandwiched between an optically thick metallic back plane and a structured metallic top nanoantenna, where totally suppressed light transmission and reflection can be achieved in an optimized structure, which leads to perfect absorption at a specific wavelength.[29–32] In this optimized MA, a well-confined and highly enhanced electromagnetic near-field in the vicinity of the top nanoantenna and the bottom back plane is induced via the

I. Hwang, M. Kim, J. Yu, Prof. J. Lee
Department of Electrical Engineering
Ulsan National Institute of Science and Technology (UNIST)
Ulsan 44919, Republic of Korea
E-mail: jongwonlee@unist.ac.kr
M. Kim, Dr. J. Lee, Dr. J.-H. Choi, Dr. S. A. Park, Dr. W. S. Chang, Dr. J.-Y. Jung
Nano-Convergence Mechanical Systems Research Division
Korea Institute of Machinery and Materials (KIMM)
Daejeon 305-343, Republic of Korea
E-mail: jjy2121@kimm.re.kr
The ORCID identification number(s) for the author(s) of this article can be found under https://doi.org/10.1002/smtd.202100277.

DOI: 10.1002/smtd.202100277

excitation of localized surface plasmon resonance. Moreover, through the near-field coupling with the vibrational mode of the analyte molecule, SEIRA signal enhancement can be achieved. To further improve SEIRA sensing capability based on MAs and extend its utility, previous studies have used an MA with a dielectric nanopedestal spacer with an increased effective sensing area[14] or the spacer itself as a fluidic[33–35] or gas channel.[36] It is generally accepted that a dielectric spacer thickness optimization to several tens to hundreds of nanometers in the mid-IR range is required to achieve near-perfect absorption and thereby obtain the maximum SEIRA signal enhancement.[21,37]

Here, we propose and experimentally demonstrate an unprecedented level of ultrasensitive molecule detection based on an MA with an undercut of an extremely thin dielectric spacer with a thickness of 10 nm to effectively form a vertical nanogap between the top nanoantenna and the bottom backplane. By employing the vertical nanogap in the MA, we can simultaneously obtain near-perfect absorption, even at a 10 nm spacer thickness, extremely high near-field intensities induced on both the revealed top and bottom metal surfaces, and a further extended effective sensing area. The top plasmonic nanoantenna array of the MAs was processed using nanoimprint lithography (NIL), and a vertical nanogap was formed using isotropic dry etching. The fabrication process proposed in this study is low cost and can produce a vertical nanogap of 10 nm in a large area.[38–40] The sensing capability of the MA with a vertical nanogap was experimentally verified using monolayer (2.8 nm thickness) molecules of 1-octadecanethiol (ODT), which is frequently used as an analyte molecule to assess the sensing capability of Au SEIRA platform,[10,13,14,41–46] and a record-high reflection difference SEIRA signal of 36% was obtained.

2. Results and Discussion

Schematics of the MA with a vertical nanogap and its unit cell structure are illustrated in **Figure 1**a,b. The unit cell structure consists of a top cross-shaped Au nanoantenna, a bottom Au backplane, and an undercut of SiO_2 dielectric spacer. For a comparative study, three different unit cell structures with three different cross-shaped antenna dimensions and dielectric spacer layer thicknesses (10, 15, and 30 nm) were used in this study, and each unit cell structure was optimized to have a plasmonic resonance near the wavelength of 3.5 μm after coating the ODT molecules on the revealed metal surface. The structural parameters of the three structures are explained in Figure 1. It is known that the target ODT molecules exhibit IR fingerprint vibrations at wavelengths of 3427 and 3509 nm, owing to their asymmetric and symmetric CH_2 stretching vibrations, respectively, and they can be coated on the Au surface in the form of a self-assembled monolayer with a thickness of 2.8 nm by thiol–metal bonding through van der Waals interactions.[47–50] Figure 1b shows a zoomed-in view of the vertical nanogap region, which depicts that the ODT molecules form a monolayer on the revealed Au surface. The MA employing the cross-shaped nanoantenna can easily tune the resonant wavelength by adjusting the length of the antenna (L); it has a relaxed light polarization sensitivity and can induce strong near-field intensity at the corner of the antenna edge. In addition, by employing the vertical nanogap, a larger dimension of the nanoantenna is required for a particular resonant wavelength, owing to the lower effective refractive index of the dielectric spacer. The revealed bottom surface of the top nanoantenna and the top surface of the bottom backplane can be additionally utilized for molecule sensing, which leads to a significantly increased effective sensing area. Figure 1c and Figure 1d show top views of scanning electron microscopy (SEM) images (top panel) and cross-sectional side views of transmission electron microscopy (TEM) images (bottom panel) of the fabricated MA with 10 and 15 nm vertical nanogaps, respectively, and the samples were cut using a focused ion beam in the vertical direction of the antenna length at ≈30 nm from the end edge of the nanoantenna. Figure 1e shows top view (top panel), tilted view (middle panel), and side view (bottom panel) of SEM images of the fabricated MA with a 30 nm vertical nanogap device. Atomic force microscope images of the MA with the 30 nm vertical nanogap sample are provided in Figure S1 (Supporting Information). In these three structures, vertical nanogaps of 10, 15, and 30 nm, which were controlled according to the thickness of the dielectric spacer, were well formed. In the case of a relatively thick top Au layer, trapezoidal cross-sectional profiles were formed during Au layer deposition. The top nanoantenna arrays were formed using the NIL process, and a vertical nanogap was formed using a plasma asher.

The use of an MA as a coupled cavity with a single port is well described by the analytic framework of the temporal coupled mode theory (TCMT) as schematically shown in **Figure 2**a. From the TCMT model, the absorption of the cavity (A) without coating of the ODT molecules ($\mu_1 = \mu_2 = 0$) is described by Equation (1), which shows that the absorption depends on the ratio of the radiation loss rate (γ_{rad}) to the absorption loss rate (γ_{abs})[37]

$$A = \frac{4\gamma_{abs}\gamma_{rad}}{(\omega-\omega_0)^2+(\gamma_{abs}+\gamma_{rad})^2} \quad (1)$$

where ω_0 is the resonant frequency of the cavity. The coupling conditions are categorized into three cases depending on the ratio of the two loss rates: critical coupling ($\gamma_{rad} = \gamma_{abs}$), which produces perfect absorption at the resonant frequency, undercoupling ($\gamma_{rad} < \gamma_{abs}$), and overcoupling ($\gamma_{rad} > \gamma_{abs}$). The radiation and absorption loss rates are mainly affected by the geometries of the cavity and constituent materials, respectively. In the application of the MA for SEIRA spectroscopy, when the two loss rates are comparable, a strong mode amplitude and near-field intensity in the cavity are induced, leading to a more enhanced SEIRA signal. If the thickness of the dielectric spacer is further reduced below its optimum value, which produces perfect absorption, the ratio of the loss rates ($\gamma_{rad}/\gamma_{abs}$) moves away from 1 ($\gamma_{rad}/\gamma_{abs} < 1$), owing to the strong gap surface plasmon resonance induced in the structure, which places the MA in a deep undercoupling regime. Accordingly, the absorption of the MA is decreased, and the near-field intensity induced in the structure is also reduced, resulting in a lower efficiency for SEIRA applications. This limitation can be addressed when employing a thick layer for the top Au nanoantenna; however, it raises the problems of high process cost and difficulty of fabrication. The MA with a vertical nanogap proposed in this study

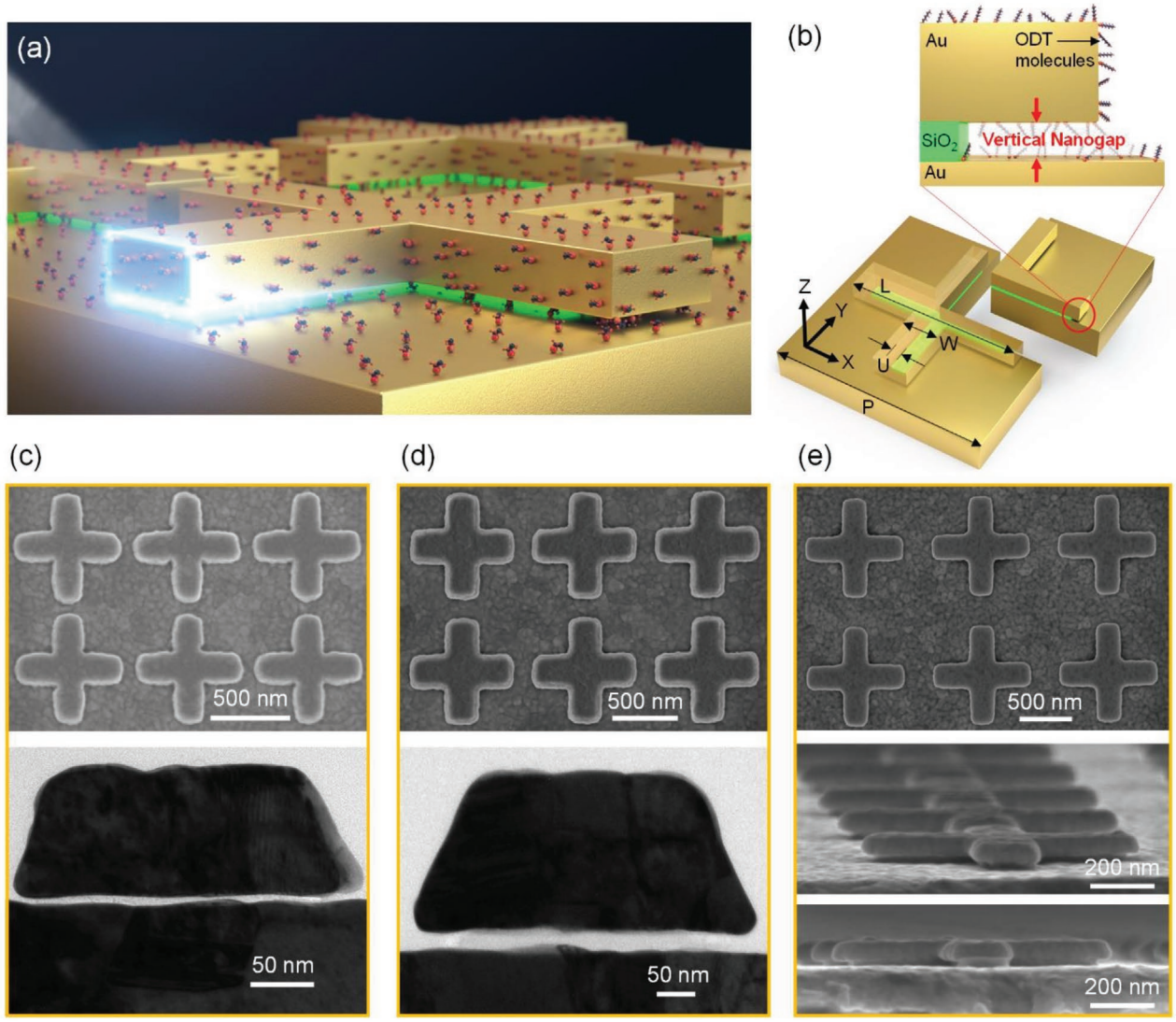

Figure 1. Schematic images of a) the MA with a vertical nanogap and its unit cell structure and b) zoomed-in image of the vertical nanocap edge portion of the MA with ODT monolayer. Top view of SEM images (top panel) and cross-sectional TEM images (bottom panel) of the processed MAs with c) 10 nm and d) 15 nm vertical nanogaps. e) Top view (top panel), tilted view (middle panel), and cross-sectional (bottom panel) view of SEM images of the processed MA with a 30 nm vertical nanogap. Structural dimensions of the MAs (in the order of 10, 15, and 30 nm vertical nanogaps) are $P = 750$, 900, 1200 nm, $L = 700$, 780, 940 nm, and $W = 170$, 250, 270 nm, thickness of the top Au nanoantenna, $t_{Au} = 90$, 100, 45 nm, $U = 50$ nm for the three structures.

can successfully address this problem and can be utilized as a sensing platform that can significantly enhance SEIRA signal. Qualitatively, the vertical nanogap through the undercut formation of SiO_2 layer interferes with the magnetic resonance coupling of the MA structure, resulting in an increase in loss rate ratio, absorption, and near-field enhancement, and, at the same time, increasing the sensing area as shown in Figure 2b. In addition to this, when the thickness of the SiO_2 layer becomes thinner, a stronger near-field enhancement is formed at the nanoantenna edge. To confirm this, numerical analysis through simulation was performed using the MA with the nanoantenna that has a rounded edge corner, referring to the SEM image of the fabricated sample. Figure 2c shows the simulation results of the radiation loss rate (left *y*-axis) and the absorption loss rate (right *y*-axis) changes, which were induced according to the undercut etch depth (*U* in Figure 1b) of the MA with the three different dielectric spacer thicknesses. The "unetched" condition in the *x*-axis indicates that the SiO_2 layer is not etched at all, and the undercut etch depth of 0 nm means that only the SiO_2 layer region, excluding the region underneath the top nanoantenna, is etched down to the bottom backplane. The loss rates were calculated by increasing the undercut etch depth by a 10 nm step in the lateral direction from 0 to 50 nm. Because the three MAs have different structural dimensions, the starting points of the two loss rates are different; however, a general trend was found in the simulation. As the undercut etch depth increased, the absorption loss rate did not change significantly, but the radiation loss rate increased rapidly. The formation of

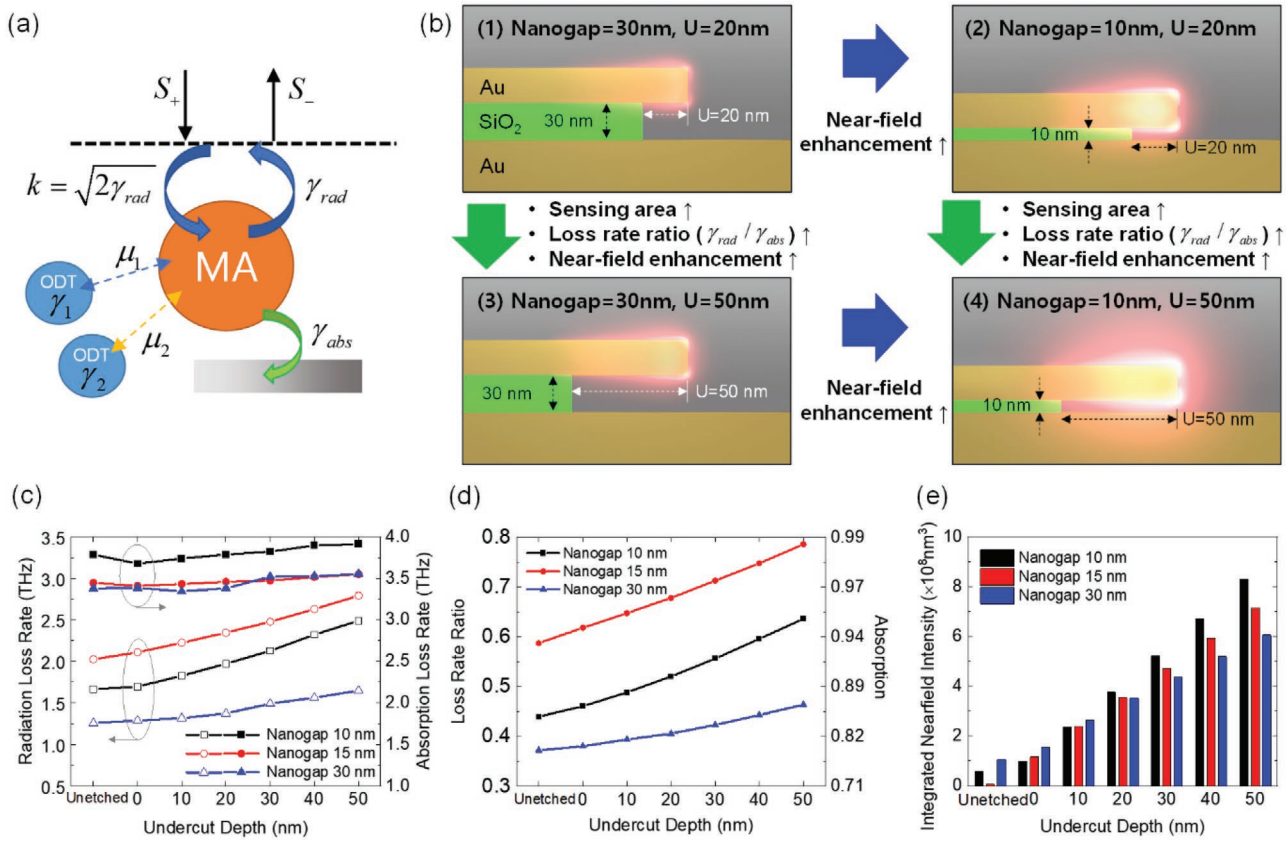

Figure 2. a) Schematic of the cavity model for TCMT analysis. b) Schematic images of the edge portion of the MA structure with near-field enhancement for various vertical nanogap thicknesses and undercut depths. c) Numerical calculation of the radiation loss rate γ_{rad} (left *y*-axis) and absorption loss rate γ_{abs} (right *y*-axis) of the three MAs for different undercut etch depths. d) Numerical calculation of the loss rate ratio $\gamma_{rad}/\gamma_{abs}$ (left *y*-axis) and absorption (right *y*-axis) of the three MAs for different undercut etch depths. e) Calculation results of the integrated near-field intensity for the three MAs for different undercut etch depths.

the undercut of the dielectric spacer interferes with the magnetic dipole resonance, which resulted in increased radiation loss. This trend can be more clearly confirmed by taking the ratio of the two loss rates ($\gamma_{rad}/\gamma_{abs}$) according to the undercut etch depth change, as shown in Figure 2d. As the undercut etch depth increased, the ratio of the two loss rates increased, and accordingly, the absorption of the three MAs increased above 0.87 according to Equation (1). As the undercut etch depth increased, the highest absorption result was obtained for the MA with a 15 nm vertical gap, where the structure was best optimized; this was followed by the 10 and 30 nm vertical nanogaps. The three MAs with similar levels of absorption can be understood as similar systems from the perspective of the TCMT model. However, when they are applied to SEIRA spectroscopy, the degree of near-field interaction with the analyte molecules varies according to the MA geometry; therefore, different sensing efficiencies can be obtained. The major factor that determines the efficiency of SEIRA sensing is the integrated near-field intensity in the sensing volume, where the analyte molecules are located. Considering the thickness of the ODT monolayer molecule, the integrated near-field intensities in the 3 nm thick air regions around the revealed Au surfaces for the three MAs with different undercut etch depths were calculated, as shown in Figure 2e. Although the three MAs have similar absorption values, as the thickness of the spacer layer becomes thinner, a larger integrated near-field intensity is induced, and it increases linearly with different increase rates as the undercut etch depth is increased. Among the three MAs, the maximum integrated near-field intensity was obtained for the MA with a 10 nm vertical nanogap at an undercut etch depth of 50 nm, which was attributed to the high near-field enhancement induced on the revealed top and bottom metal surfaces by a strong surface plasmon resonance in the air gap region. The simulation results of the reflection spectra according to the undercut etch depth for the three MAs are shown in Figure S2 (Supporting Information). In addition, the integrated near-field intensities induced on the revealed surfaces of the top Au nanoantenna and bottom Au backplane are provided separately in Figure S3 (Supporting Information), which shows that in the case of a thinner spacer, significant near-field intensity is induced on the surfaces of both the top Au nanoantenna and the bottom Au backplane. The near-field enhancement (E/E_0) formed in the three MAs with an undercut etch depth of 50 nm was monitored from the top view (top panel) at the interface of the top nanoantenna and SiO_2 spacer and from the vertical cross-sectional view (bottom panel) along the red dotted line of the long arm of the cross nanoantenna, as shown in **Figure 3**a–c. In the three MAs, over 80 strong

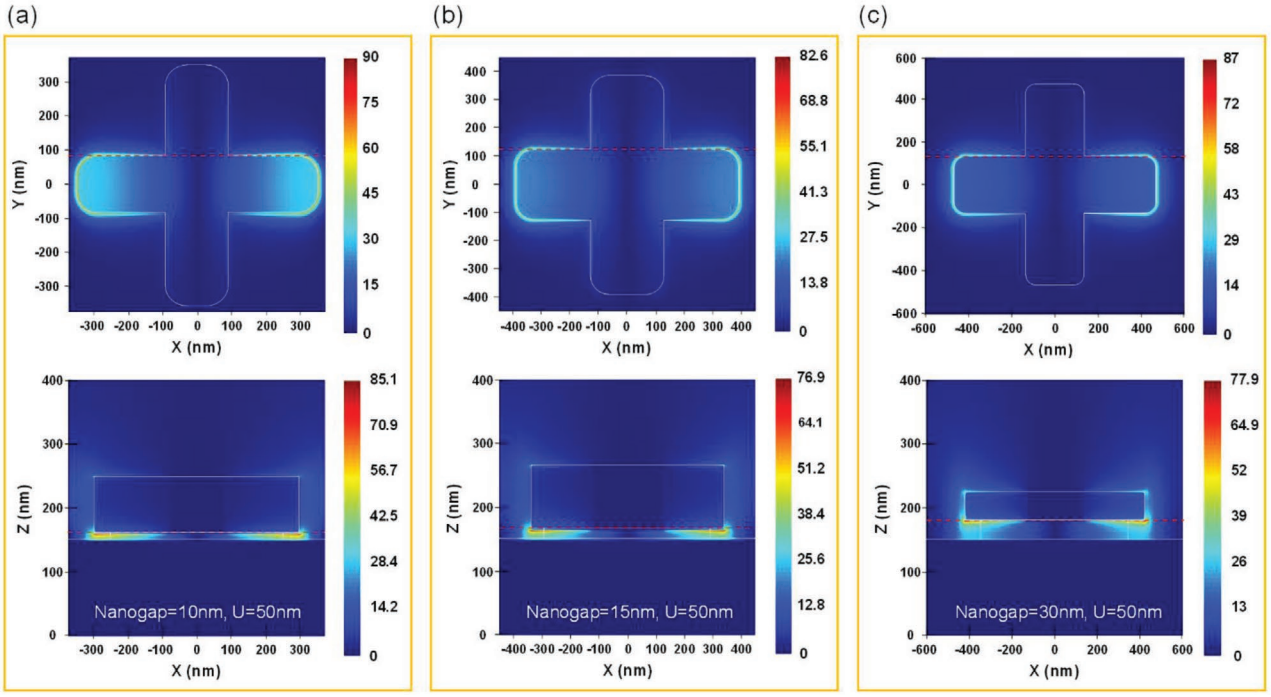

Figure 3. Top view (top panel) and cross-sectional view (bottom panel) of the simulated near-field enhancement (E/E_0) profile for the MA structure with a) 10 nm, b) 15 nm, and c) 30 nm vertical nanogaps monitored at resonance for each structure.

near-field enhancements were formed at the edge corners of the top nanoantenna. As the dielectric spacer thickness decreased, a higher and more uniform near-field enhancement was formed in the air gap region between the top and bottom metal layers. The near-field enhancement uniformly distributed over the vertical nanogap induces stronger vibrational mode coupling with the analyte molecule; this suggests that increased SEIRA signal sensitivity can be obtained. To directly confirm the SEIRA sensing characteristics, the reflection spectra of the MA with a vertical nanogap structure, coated with a 3 nm thick ODT monolayer, were obtained through numerical simulation, and the results are shown in **Figure 4**. Figure 4a and Figure 4b show the reflection spectra and the reflection difference SEIRA signal of ODT, respectively, which were extracted by subtracting the baseline from the asymmetric least-squares smoothing (AsLSS) algorithm[51] for the MA structure with a 10 nm vertical nanogap for the five different undercut etch depths. In the designed nanoantenna structure, the spectral blueshift and the increase in the SEIRA signal can be clearly observed as the undercut etch depth increases. Figure 4c and Figure 4d show the reflection spectra and reflection difference SEIRA signal according to the thicknesses of the dielectric spacer at the undercut etch depth of 50 nm, respectively. As the thickness of the dielectric spacer decreases, an increased SEIRA signal is obtained, which is in good agreement with the trend of the integrated near-field intensity shown in Figure 2e.

For an experimental demonstration of the proposed concept, MAs with vertical nanogap sizes of 1×1 mm^2 were fabricated using NIL and isotropic dry-etching processes (see the "Experimental Section" for the fabrication details). We attempted several isotropic dry-etching methods to form vertical nanogaps for the MAs. Inductive coupled plasma (ICP) etching with a forward power of 0 W, which is an isotropic dry-etching method,[52,53] was used to form the vertical nanogap of the MA. In addition, the reactive ion etching (RIE) method was used to undercut the SiO_2 dielectric layer. Partial removal of the SiO_2 dielectric layer induces blueshifted reflection spectra, owing to the reduction of the effective index of the dielectric spacer. Thus, through blueshifts of the measured reflection spectra, the vertical nanogap of the MA can be indirectly confirmed. Even though the blueshifts of the measured reflection spectra for the etched MAs by both ICP etching and RIE were confirmed, the proper vertical nanogaps of the MAs failed, as shown in Figure S4 (Supporting Information). Finally, a plasma asher with the proper conditions was used to form the vertical nanogap of the MA. The reflection spectra of the MA etched by the plasma asher were measured according to the undercut etching time and were blueshifted (cf. Figure S5, Supporting Information).

For the experimental validation of the sensing capability of the three MAs with vertical nanogaps, we prepared three MA samples with the ODT monolayer for SEIRA sensing. To form a self-assembled monolayer of ODT molecules on the revealed Au surface, the devices were immersed in 1 mmol ODT solution diluted in absolute ethanol for 24 h. They were then rinsed in ethanol to remove the ODT residue that did not contribute to the monolayer. Finally, the samples were carefully dried using a nitrogen blow. IR reflection spectra were measured using an FTIR spectrometer equipped with an IR microscope under unpolarized IR illumination. The reflection spectra were obtained by properly normalizing the signal from the MA array to that from the bare Au surface. We used a spectral resolution

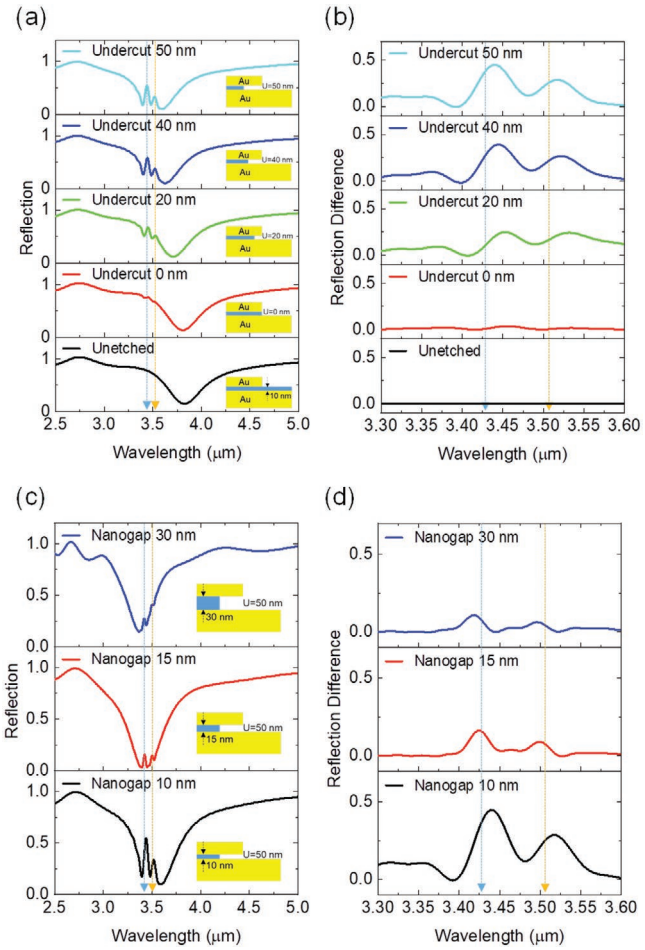

Figure 4. a) Simulated reflection spectra and b) reflection difference SEIRA signal of the ODT-coated MA with a 10 nm vertical nanogap for different undercut etch depths. The blue and orange vertical lines indicate the two vibrational absorption peaks of the ODT molecule. c) Simulated reflection spectra and d) the reflection difference SEIRA signal of the ODT-coated MA with 30, 15, and 10 nm vertical nanogaps with an undercut etch depth of 50 nm.

of 4 cm^{-1} with 64 scans. **Figure 5**a shows the experimental reflection spectra before (black) and after (red) the coating of the ODT monolayer for the 30 nm (top panel), 15 nm (middle panel), and 10 nm (bottom panel) vertical nanogaps. Subsequent to the ODT monolayer coating, a spectral redshift was observed for all three MAs, owing to the increased effective refractive index around the structure. In addition, as the spacer thickness decreased, a larger redshift effect was observed, which indicates that the structure responds more sensitively to the surrounding refractive index. The blue and orange dashed lines in Figure 5a indicate the asymmetric (3.427 μm) and symmetric (3.509 μm) CH_2 vibrational wavelengths of the ODT molecules, respectively. The SEIRA signal of the electromagnetic-induced-transparency (EIT) type was obtained at the two absorption wavelengths of the ODT molecule, and the largest SEIRA signal was observed in the 10 nm vertical nanogap sample. The EIT-type SEIRA signal occurs in the MA located in the undercoupling regime. To extract the SEIRA signal in the form of reflection difference, the baseline (blue dotted line) was calculated using the AsLSS algorithm, and the reflection signal difference between the baseline and the original spectra was obtained, as shown in Figure 5b. The 30, 15, and 10 nm vertical nanogap samples obtained reflection difference SEIRA signals of 0.12, 0.22, and 0.36 at a wavelength of 3.427 μm, respectively, and SEIRA signals of 0.08, 0.15, and 0.21 at a wavelength of 3.509 μm, respectively. Notably, the 10 nm vertical nanogap sample obtained the largest spectral signal among the SEIRA studies using the ODT monolayer reported to date (cf. Table S1, Supporting Information). We note that the maximum SEIRA signal can be obtained when the ODT vibrational absorption peaks are located near the absorption peak of the ODT-coated MA (cf. Figure S6, Supporting Information). The proposed structure can be applied to the detection of a larger size of molecule than ODT by adjusting the size of vertical nanogap. In this case, even in the MA with an increased nanogap size, a strong SEIRA sensing signal can be obtained as the near-field integration volume increases (cf. Figure S7, Supporting Information).

For a quantitative analysis of the experimental results, spectral fitting and physical parameter extraction were conducted using the experimental reflection spectra of the ODT-coated MA with a vertical nanogap and the reflection TCMT model derived from a system in which two vibrational modes of the ODT molecule are coupled with an MA with a vertical nanogap ($\mu_1 \neq 0$, $\mu_2 \neq 0$, cf. Figure 2a). From our previous study, the analytic equation of the reflection (R) can be expressed as follows[14]

$$R = 1 - \frac{4\gamma_{\mathrm{rad}}\left(\gamma_{\mathrm{abs}} + \gamma_{\mu 1} + \gamma_{\mu 2}\right)}{\left(\omega - \omega_0 - \omega_{\mu 1} - \omega_{\mu 2}\right)^2 + \left(\gamma_{\mathrm{rad}} + \gamma_{\mathrm{abs}} + \gamma_{\mu 1} + \gamma_{\mu 2}\right)^2} \quad (2)$$

where ω_0 is the resonant frequency of the ODT-coated MA with a vertical nanogap, $\gamma_{\mu i} = \mu_i^2\gamma_i/[(\omega-\omega_i)^2+\gamma_i^2]$ and $\omega_{\mu i} = \mu_i^2(\omega-\omega_i)/[(\omega-\omega_i)^2+\gamma_i^2]$ are the effective loss rate and modified vibrational frequency of the ODT molecule for the asymmetric (i = 1) and symmetric (i = 2) vibrations, respectively, where ω_i ($\omega_1 = 5.5 \times 10^{14}$ rad s^{-1} and $\omega_2 = 5.37 \times 10^{14}$ rad s^{-1}) and γ_i($\gamma_1 = 2.5 \times 10^{12}$ rad s^{-1} and $\gamma_2 = 1.8 \times 10^{12}$ rad s^{-1}) are the resonant frequency and the damping rate of the ODT molecule, respectively; μ_i is the coupling rate that reflects the direct energy exchange between the ODT vibrational mode and the cavity mode of the MA. By fitting the experimental data with the TCMT model (cf. Figure S8, Supporting Information), the 30, 15, and 10 nm vertical nanogap samples obtained coupling rates μ_1 of 4.46×10^{12}, 7.10×10^{12}, and 9.24×10^{12} rad s^{-1} at a wavelength of 3.427 μm, respectively, and coupling rates μ_2 of 2.93×10^{12}, 4.08×10^{12}, and 5.59×10^{12} rad s^{-1} at a wavelength of 3.509 μm, respectively. The coupling rate is a major factor that is directly related to the integrated near-field intensity induced in the MA with a vertical nanogap and determines the degree of SEIRA signal enhancement. Table S2 (Supporting Information) shows the results of the coupling rates extracted by fitting the measured reflection spectra using the TCMT model. The results are consistent with those expected from the above integrated near-field intensity results, and the largest coupling rates were obtained in the MA with a 10 nm vertical nanogap. It is noted that simultaneous detection of absorption peaks of analytes having various functional groups such as biomolecules

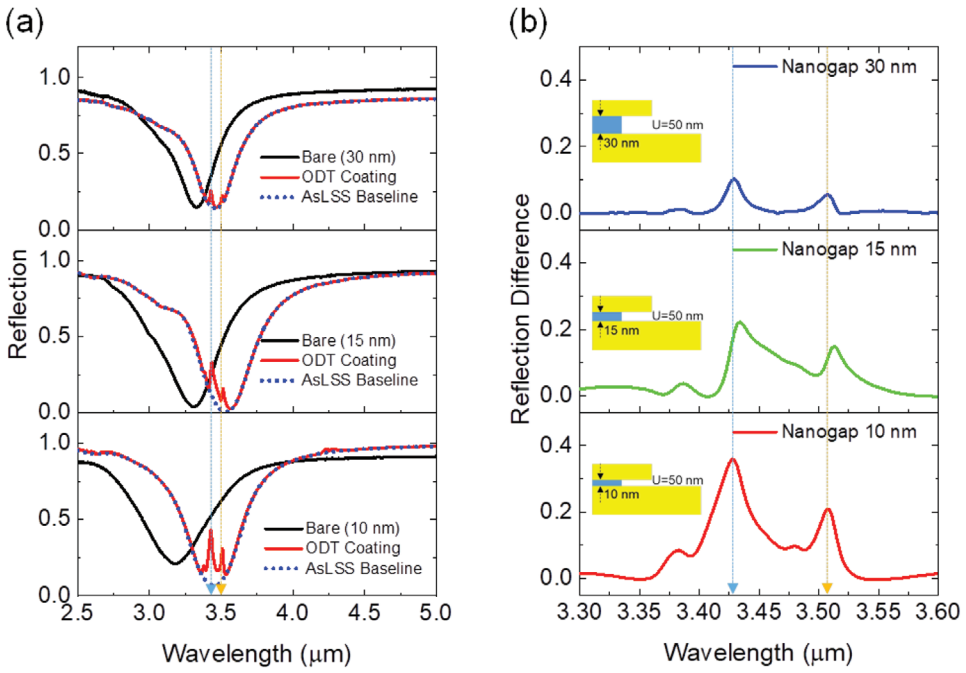

Figure 5. a) Measured reflection spectra of the MA with 30 nm (top panel), 15 nm (middle panel), and 10 nm (bottom panel) vertical nanogaps before (black) and after (red) ODT coating. The blue-dotted curve indicates the numerically calculated baseline using the AsLSS algorithm, and the blue and orange vertical lines indicate the two vibrational absorption peaks of the ODT molecule. b) Measured reflection difference SEIRA signal for the MA with 30 nm (top panel), 15 nm (middle panel), and 10 nm (bottom panel) vertical nanogap structures.

is possible through the use of a plasmonic antenna structure with multimodal resonances[21] or a supercell structure using antennas of different sizes.[54]

3. Conclusion

We proposed and experimentally demonstrated ultrasensitive molecule detection based on an MA with a 10 nm thick vertical nanogap for the SEIRA detection platform. To compare and verify the sensing capability using an ODT monolayer, MAs with three different vertical nanogap thicknesses were theoretically and experimentally analyzed, and a record-high reflection difference SEIRA signal of 36% was obtained in the smallest 10 nm thick vertical nanogap. The reflection difference SEIRA signal was analyzed through a numerical simulation of the integrated near-field intensity and TCMT analytic model. The proposed SEIRA platform can be produced in a cost-efficient large area using NIL and isotropic dry-etching processes and can appeal to biosensing applications that require high sensitivity and selectivity. Owing to the high sensitivity of minute amounts of analyte molecules, the proposed structure may be potentially applicable to gas-sensing applications, which our research team is currently researching.

4. Experimental Section

Numerical Calculation: Finite-difference time-domain (FDTD) calculations were performed using commercial software (Lumerical FDTD Solutions, 2020a). The optical properties for each unit cell of the three plasmonic MAs were calculated by applying boundary conditions that are antisymmetric along the *x*-direction, symmetric along the *y*-direction, and a perfectly matched layer along the *z*-direction. The integrated near-field intensities and electric field profiles at only the resonance wavelength under the *x*-polarized plane wave were calculated. The integrated near-field intensities were calculated using data collected from 3D index and field monitors. All element values from the electric field monitor, excluding conformal points that were 3 nm from the gold–air boundary, were processed as 1; all other points were converted to 0. The integrated near-field intensities were calculated as the sum of the product of the elements of the processed indices and the values of the squared electric fields. The unit structure was simulated with a local mesh $x = y = z = 1$ nm, and a 1×10^{-7} auto-shutoff level to optimize runtime, collect data, and conduct precise calculations to consider the 3 nm thickness of the adsorbed ODT monolayer. Due to the limitation of computational capacity, 1 nm was the minimum mesh size, and 3 nm thickness of ODT was used for numerical simulation only, not 2.8 nm of the actual ODT thickness. The imaginary part of the dielectric constant of the ODT molecule was doubled for the appearance of a distinct molecular vibration peak. The unit structure is composed of the top metal and silicon dioxide as a "rectangular polygon with rounded corners" in the embedded components group. The radius of the edges of the top metal was 60 nm, and the radius of SiO_2 was determined by ((60 nm/width of metal) × (width of SiO_2)) under the change of the laterally undercut etch depth. The resolution of the rounded corners was applied with 1000 vertices to approximate roundness. The baselines of the simulated and measured spectra were applied using embedded AsLSS in the DataAnalysis group of the graphing software (Origin Pro 2020). The asymmetric factor was set to 1×10^{-7} for positive peaks to specify the weight of the points above the baseline in each iteration. The smaller the threshold, the more points above the baseline will be excluded to determine the baseline in the next iteration. The threshold was set to 0.01 to determine the ratio of the critical distance of the point to the baseline to that of the positive peaks to the baseline. The smoothing factor and number of iterations were set to 3.3 and 8, respectively.

Device Fabrication: For the NIL process, Si masters with three different sizes of cross-antenna pattern arrays were prepared using standard

electron-beam lithography and the RIE process. To fabricate the MAs, the pattern array on the Si master was transferred onto a polyurethane–acrylate (PUA) mold film. Three Si wafers with a 10/150 nm thick chromium (Cr)/Au bottom metal layer were deposited by electron-beam evaporation, and SiO_2 layers with thicknesses of 10, 15, and 30 nm were deposited on the wafer using plasma-enhanced chemical vapor deposition. For the pattern transfer using NIL, the LOR1A lift-off resist (MicroChem) and LV400 resist (UV curable Si-based resist, Chemoptics) were coated on the prepared Si wafer. The pattern array on the PUA mold film was then transferred onto the Si wafer using the UV NIL process at a pressure of 3 bar under a UV exposure time of 95 s. The residual layer of the LV400 resist was removed by RIE using a gas mixture of CF_4 and O_2 at an radio frequency power of 100 W, and the MA array patterned LOR1A resist layer with an undercut profile was formed by O_2 RIE at an RF power of 50 W. A 5 nm thick Cr layer and Au layer with different thicknesses (90, 100, and 70 nm thicknesses of Au for 10, 15, and 30 nm vertical nanogaps, respectively) were deposited on the sample, which was followed by the lift-off to form the cross-antenna-shaped array on the SiO_2 layer. The undercut of the SiO_2 layer was processed through isotropic dry etching using a gas mixture of 10 sccm of O_2 and 30 sccm of CF_4 at 300 W of RF power, and the undercut etch depth was controlled using the isotropic dry-etching time.

Supporting Information

Supporting Information is available from the Wiley Online Library or from the author.

Acknowledgements

This work was supported by the Nano-Material Technology Development Program through the National Research Foundation of Korea (NRF) grant funded by the Korean government (MSIT) (Grant No. 2018M3A7B4069995), the Center for Advanced Meta-Materials (CAMM) grant funded by the Korean government (MSIT) as a Global Frontier Project (Grant No. 2014M3A6B3063700), and by the Institute of Civil Military Technology Cooperation grant funded by the Defense Acquisition Program Administration and Ministry of Trade, Industry and Energy of Korean government (Grant No. 18-CM-SS-17). This work was also supported by the Korea Institute of Machinery and Materials under Grant No. NK232E.

Conflict of Interest

The authors declare no conflict of interest.

Data Availability Statement

The data that support the findings of this study are available from the corresponding authors upon reasonable request.

Keywords

infrared vibrations, metamaterials, nanoimprint lithography, plasmonics, surface-enhanced infrared absorption spectroscopy

Received: March 11, 2021
Revised: April 22, 2021
Published online: May 13, 2021

[1] J. M. Chalmers, P. R. Griffiths, *Handbook of Vibrational Spectroscopy*, John Wiley & Sons Ltd., Chichester, UK **2002**.
[2] K. Ataka, T. Kottke, J. Heberle, *Angew. Chem., Int. Ed.* **2010**, *49*, 5416.
[3] F. Neubrech, A. Pucci, T. W. Cornelius, S. Karim, A. Garcia-Etxarri, J. Aizpurua, *Phys. Rev. Lett.* **2008**, *101*, 157403.
[4] R. Adato, S. Aksu, H. Altug, *Mater. Today* **2015**, *18*, 436.
[5] F. Neubrech, C. Huck, K. Weber, A. Pucci, H. Giessen, *Chem. Rev.* **2017**, *117*, 5110.
[6] T. G. Mayerhöfer, J. Popp, *Nanophotonics* **2017**, *7*, 39.
[7] X. X. Yang, Z. P. Sun, T. Low, H. Hu, X. D. Guo, F. J. G. de Abajo, P. Avouris, Q. Dai, *Adv. Mater.* **2018**, *30*, 1704896.
[8] E. Cubukcu, S. Zhang, Y. S. Park, G. Bartal, X. Zhang, *Appl. Phys. Lett.* **2009**, *95*, 043113.
[9] L. V. Brown, X. Yang, K. Zhao, B. Y. Zheng, P. Nordlander, N. J. Halas, *Nano Lett.* **2015**, *15*, 1272.
[10] C. Huck, J. Vogt, M. Sendner, D. Hengstler, F. Neubrech, A. Pucci, *ACS Photonics* **2015**, *2*, 1489.
[11] G. Pellegrini, L. Baldassare, V. Giliberti, J. Frigerio, K. Gallacher, D. J. Pau, G. Isella, M. Ortolani, P. Biagioni, *ACS Photonics* **2018**, *5*, 3601.
[12] A. E. Cetin, D. Etezadi, H. Altug, *Adv. Opt. Mater.* **2014**, *2*, 866.
[13] C. Huck, A. Toma, F. Neubrech, M. Chirumamilla, J. Vogt, F. De Angelis, A. Pucci, *ACS Photonics* **2015**, *2*, 497.
[14] I. Hwang, J. Yu, J. Lee, J. H. Choi, D. G. Choi, S. Jeon, J. Lee, J. Y. Jung, *ACS Photonics* **2018**, *5*, 3492.
[15] Y. Jung, I. Hwang, J. Yu, J. Lee, J. H. Choi, J. H. Jeong, J. Y. Jung, J. Lee, *Sci. Rep.* **2019**, *9*, 7834.
[16] X. S. Chen, C. Ciraci, D. R. Smith, S. H. Oh, *Nano Lett.* **2015**, *15*, 107.
[17] D. Yoo, D. A. Mohr, F. Vidal-Codina, A. John-Herpin, M. Jo, S. Kim, J. Matson, J. D. Caldwell, H. Jeon, N. C. Nguyen, L. Martin-Moreno, J. Peraire, H. Altug, S. H. Oh, *Nano Lett.* **2018**, *18*, 1930.
[18] D. Yoo, F. de Leon-Perez, M. Pelton, I. H. Lee, D. A. Mohr, M. B. Raschke, J. D. Caldwell, L. Martin-Moreno, S. H. Oh, *Nat. Photonics* **2021**, *15*, 125.
[19] A. Tittl, A. Leitis, M. K. Liu, F. Yesilkoy, D. Y. Choi, D. N. Neshev, Y. S. Kivshar, H. Altug, *Science* **2018**, *360*, 1105.
[20] A. Leitis, A. Tittl, M. K. Liu, B. H. Lee, M. B. Gu, Y. S. Kivshar, H. Altug, *Sci. Adv.* **2019**, *5*, eaaw2871.
[21] K. Chen, R. Adato, H. Altug, *ACS Nano* **2012**, *6*, 7998.
[22] Y. Q. Li, L. Su, C. Shou, C. M. Yu, J. J. Deng, Y. Fang, *Sci. Rep.* **2013**, *3*, 2865.
[23] K. Chen, T. D. Dao, S. Ishii, M. Aono, T. Nagao, *Adv. Funct. Mater.* **2015**, *25*, 6637.
[24] A. Ishikawa, T. Tanaka, *Sci. Rep.* **2015**, *5*, 12570.
[25] T. G. Mayerhofer, R. Kninper, U. Hubner, D. Cialla-May, K. Weber, H. G. Meyer, J. Popp, *ACS Photonics* **2015**, *2*, 1567.
[26] A. E. Cetin, S. Korkmaz, H. Durmaz, E. Aslan, S. Kaya, R. Paiella, M. Turkmen, *Adv. Opt. Mater.* **2016**, *4*, 1274.
[27] F. B. Barho, F. Gonzalez-Posada, M. Bomers, A. Mezy, L. Cerutti, T. Taliercio, *ACS Photonics.* **2019**, *6*, 1506.
[28] L. V. Brown, K. Zhao, N. King, H. Sobhani, P. Nordlander, N. J. Halas, *J. Am. Chem. Soc.* **2013**, *135*, 3688.
[29] N. I. Landy, S. Sajuyigbe, J. J. Mock, D. R. Smith, W. J. Padilla, *Phys. Rev. Lett.* **2008**, *100*, 207402.
[30] X. L. Liu, T. Starr, A. F. Starr, W. J. Padilla, *Phys. Rev. Lett.* **2010**, *104*, 207403.
[31] C. M. Watts, X. L. Liu, W. J. Padilla, *Adv. Mater.* **2012**, *24*, Op98.
[32] J. Y. Jung, J. Lee, D. G. Choi, J. H. Choi, J. H. Jeong, E. S. Lee, D. P. Neikirk, *IEEE Photonics J.* **2015**, *7*, 1.
[33] T. H. H. Le, T. Tanaka, *ACS Nano* **2017**, *11*, 9780.
[34] T. H. H. Le, A. Morita, K. Mawatari, T. Kitamori, T. Tanaka, *ACS Photonics* **2018**, *5*, 3179.
[35] J. Xu, Z. Ren, B. Dong, X. Liu, C. Wang, Y. Tian, C. Lee, *ACS Nano* **2020**, *14*, 12159.
[36] D. S. Su, D. P. Tsai, T. J. Yen, T. Tanaka, *ACS Sens.* **2019**, *4*, 2900.
[37] R. Adato, A. Artar, S. Erramilli, H. Altug, *Nano Lett.* **2013**, *13*, 2584.
[38] M. Rumler, M. Foerthner, L. Baier, P. Evanschitzky, M. Becker, M. Rommel, L. Frey, *Nano Futures* **2017**, *1*, 015002.

[39] S. Sung, C. H. Kim, J. Lee, J. Y. Jung, J. H. Jeong, J. H. Choi, E. S. Lee, *Int. J. Precis. Eng. Manuf. - Green Technol.* **2014**, *1*, 25.
[40] C. Wang, Q. Zhang, Y. Song, S. Y. Chou, *ACS Nano* **2014**, *8*, 2618.
[41] A. Pucci, F. Neubrech, D. Weber, S. Hong, T. Toury, M. L. de la Chapelle, *Phys. Status Solidi B* **2010**, *247*, 2071.
[42] S. Bagheri, H. Giessen, F. Neubrech, *Adv. Opt. Mater.* **2014**, *2*, 1050.
[43] X. H. Chen, C. Wang, Y. Yao, C. Wang, *ACS Nano* **2017**, *11*, 8034.
[44] D. X. Ji, A. Cheney, N. Zhang, H. M. Song, J. Gao, X. Zeng, H. F. Hu, S. H. Jiang, Z. F. Yu, Q. Q. Gan, *Adv. Opt. Mater.* **2017**, *5*, 1700223.
[45] J. Paul, S. G. McMeekin, R. M. De La Rue, N. P. Johnson, *Sens. Actuators, A* **2018**, *279*, 36.
[46] M. C. Giordano, M. Tzschoppe, M. Barelli, J. Vogt, C. Huck, F. Canepa, A. Pucci, F. B. de Mongeot, *ACS Appl. Mater. Interfaces* **2020**, *12*, 11155.
[47] D. D. Popenoe, *Ph.D. Thesis*, Iowa State University **1992**.
[48] M. D. Porter, T. B. Bright, D. L. Allara, C. E. D. Chidsey, *J. Am. Chem. Soc.* **1987**, *109*, 3559.
[49] C. D. Bain, E. B. Troughton, Y. T. Tao, J. Evall, G. M. Whitesides, R. G. Nuzzo, *J. Am. Chem. Soc.* **1989**, *111*, 321.
[50] F. Schreiber, *Prog. Surf. Sci.* **2000**, *65*, 151.
[51] P. H. C. Eilers, *Anal. Chem.* **2003**, *75*, 3631.
[52] C. C. Chen, A. Ishikawa, Y. H. Tang, M. H. Shiao, D. P. Tsai, T. Tanaka, *Adv. Opt. Mater.* **2015**, *3*, 44.
[53] Y. Moritake, T. Tanaka, *Sci. Rep.* **2017**, *7*, 6726.
[54] X. L. Liu, T. Tyler, T. Starr, A. F. Starr, N. M. Jokerst, W. J. Padilla, *Phys. Rev. Lett.* **2011**, *107*, 045901.